doi:10.1038/nature09424

Supplementary Methods

Electrophysiology

Retinas were obtained and recorded as described previously [1,2]. Briefly, eyes were taken from terminally anesthetized macaque monkeys (*Macaca mulatta, Macaca fascicularis*) euthanized by other laboratories, in accordance with Salk Institute IACUC guidelines for the care and use of animals. Immediately after enucleation, the anterior portion of the eye and vitreous were removed in room light. Segments of peripheral (6-9 mm temporal) retina that were well attached to the pigment epithelium were dissected and placed flat, RGC side down, on a planar array of extracellular microelectrodes. Two different electrode arrays equipped with custom designed integrated circuits were used. One consisted of 512 electrodes with 60 μm spacing, covering a rectangular region 1890 μm x 900 μm [3]. The second consisted of 519 electrodes with 30 μm spacing, covering a hexagonal region 450 μm on a side. Attachment to the pigment epithelium was preserved during dissection [4]. In some preparations the choroid was largely removed, up to Bruch's membrane. While recording, the retina was perfused with Ames' solution (31-36 ˚C) bubbled with 95% O_2 and 5% CO_2, pH 7.4.

Recordings were analyzed offline to isolate the spikes of different cells, as described previously [2,3]. Briefly, candidate spike events were detected using a threshold on each electrode, and the voltage waveforms on the electrode and nearby electrodes around the time of the spike were extracted. Clusters of similar spike waveforms were identified as candidate neurons if they exhibited a refractory period and an average rate greater than 0.25 Hz. Duplicate recordings of the same cell were identified by temporal cross-correlation and removed.

Light calibration

The optically reduced image of a gamma-corrected cathode ray tube computer display (Sony Multiscan E100) refreshing at 120 Hz was focused on the photoreceptor outer segments. Light intensity was controlled by neutral density filters in the light path. The emission spectrum of each display primary was measured with a PR-701 spectroradiometer (PhotoResearch, Chatsworth, CA) after passing through the optical elements between the display and the retina. The mean photoisomerization rates for the L, M and S cones were estimated by computing the inner product of the power scaled emission spectra per unit area with the spectral sensitivity of each opsin, respectively, and multiplying by the effective collecting area of primate cones (0.37 μm^2) [5]. The power of each display primary was measured at the preparation with a calibrated photodiode (UDT Instruments, San Diego, CA). The photoisomerization rates for the L, M, and S cones were approximately 2200, 2200, 900 photoisomerizations per cone per second. These estimates were not corrected for the angle of illumination and pigment self screening in the cone outer segments because the precise angle of illumination and the amount of bleached pigment were unknown. Also, estimates of the pigment density of cones vary by roughly a factor of 2. However, assuming axial rather than transverse illumination, and self-screening with a cone pigment density of 0.17 [5] changed the calculated photoisomerization rates by less than 50%.

Receptive field measurements

A white noise stimulus, composed of a lattice of square pixels updating randomly and independently of one another over time, was used to characterize the spatial, temporal and chromatic response properties of recorded RGCs [6]. The intensity of each display primary at each pixel location was chosen independently of the other primaries from a binary distribution at each refresh. The contrast of each primary (difference between the maximum and minimum intensities divided by the sum) was 96%. For low spatial resolution RF maps, the pixels were either 60 or 120 μm on a side, the stimulus refresh rate was 30 or 120 Hz, and recording duration was 15-30 minutes. For high resolution mas (Fig. 1a, surrounding panels), the pixels were 5-6 μm on a side, the stimulus refresh rate was 15, 20, or 30 Hz, and recording duration was 30-240 minutes.

In some experiments, cone isolating stimuli were used to estimate the summed contribution of all cones of each type at each pixel location (i.e. Fig. 4e) [2]. The stimulus consisted of spatiotemporal white noise with each pixel presenting either an increment or decrement of activation of only one cone type on each refresh, using silent substitution of display primaries [7]. Pixels were either 60 or 120 μm on a side, the stimulus refresh rate was 30 or 120 Hz, and the recording duration was 60 min. The contrast of the cone isolating increments and decrements was 10% for each cone type. The quality of cone isolation was checked by producing "filter-isolating" stimuli for three sets of glass filters with spectral properties similar to the spectral sensitivities of the cones (L: Oriel59500 and Schott BG-40; M: Schott VG-9; S: Oriel 59814 and Oriel 59080) [1,2]. The power of transmitted light through each filter set with each filter-isolating stimulus was then measured using a calibrated photodiode (UDT Instruments, San Diego CA). Stimuli intended to isolate each filter group yielded photodiode power measurement ratios in excess of 50:1 in the isolated compared to the nulled filter set, indicating accurate spectral calibration and cone isolation. The net contribution of each cone type to the response of each RGC was estimated by summing signals from the isolated cone type in a 5x5 pixel window around the strongest pixel of the STA, if the signal at those pixels exceeded 3 SDs of the noise measured at outlying locations. This measurement window typically included all of the RF center and a majority of the RF surround volume, while excluding pixels with little or no input from the specified cone type.

The net cone input to the center and surround of ON and OFF midget cells was summarized in Fig. 4e [8], for 263 cells from one preparation at 6.75 mm temporal eccentricity along the horizontal meridian. The ordinate indicates L/(|L|+|M|+|S|), where L represents the total L cone input to the cell summed across the RF, and similarly for M and S. The abscissa indicates M/(|L|+|M|+|S|). Cells represented by points on the diagonal boundaries received no S cone input. Cells in the upper right and lower left quadrants did not exhibit L/M cone opponent responses. Cells in the other quadrants exhibited L/M cone opponent responses.

Receptive field fits and cell type classification

For cell type classification, RFs were summarized by fitting the STA with a parametric model [2,9]. The model consisted of the product of three functions: spatial, temporal and chromatic. The

temporal function was a difference of lowpass filters. The spatial function consisted of a difference of two 2-dimensional elliptical Gaussian functions (center and surround, respectively); the angle of orientation and center positions of the two Gaussians were identical and diameter of the surround was twice that of the center. The chromatic function consisted of two scalars representing the relative sensitivity to the three display primaries. Several parameters of the center component of the fits were extracted to visualize the RF: the midpoint, the SD along the major and minor axes, and the angle of the major axis. These parameters defined an ellipse for each cell representing the 1 SD contour of the center Gaussian (Fig 1a, center). Parameters of these fits (e.g. RF radius) also aided in cell type classification (Fig 1a, center). Correspondences between functionally defined RGC types and the morphologically distinct parasol, midget and small bistratified cells were inferred based on cell densities and light response properties, as described previously [2].

Cone imaging and alignment to receptive fields

Putative cone locations identified in high resolution STAs were verified by comparing STAs with fluorescence images of cone inner and outer segments (Fig. 1b). The comparison required removing the RPE prior to recording. This step reduced the ability of cones to recover from bleaching, so it was only employed in a subset of experiments. Cones were labeled with the lectin peanut agglutinin (PNA) conjugated to the fluorescent indicator Alexa 488 (Invitrogen, Carlsbad, CA, USA). Prior to mounting on the electrode array, retinas were incubated for 10 to 30 minutes in Ames medium containing approximately 10 µg/mL PNA. Following the recording, two images were taken to register the labeled cones with the stimulus display. The first was a fluorescence image of PNA labeling of cone inner and outer segments. The second was a transmitted light image of a single white noise frame in the plane of the cones.

Cone identification and classification

Cone inputs to RGCs were estimated quantitatively by fitting a model to the fine spatial resolution white noise data. The model specified cone locations, cones types, and the strength of the input from each cone to each RGC. Thus, the model described how the cone lattice was sampled by the entire collection of RGCs. Model parameters were chosen to maximize the posterior probability of the data, a value which combines the likelihood (how well the model matched the data) with prior knowledge about the lattice of cones from previous work.

In the model, the spatial sensitivity of each cone was defined as a Gaussian profile, with a chromatic sensitivity (L, M, or S) given by the expected sensitivity of that cone type to the three display primaries. Each STA was described as a weighted sum of individual cones. Thus, the model described RGC sensitivity in space, time, and color:

$$k_i(\mathbf{x},t,c) = r_i(t)\sum_j a_{ij} f_j(c) w(\mathbf{x}-\mathbf{x}_j) \qquad (1)$$

where k_i is the i-th RF, $r_i(t)$ is the response time course, $\boldsymbol{x}_j$ is the location of the j-th cone, w is the shape of the cone RF (the same for all cones), $f_j(c)$ is the color profile (a 3 dimensional vector) of the j-th cone, and a_{ij} is the sampling strength of the j-th cone by the i-th RF. The RF was assumed to be space-time separable, a reasonable approximation because the small delay between center and surround was masked by the slow refresh of the stimulus (15-30 Hz). Control experiments indicated that the results were unchanged with a stimulus refreshing at 120 Hz.

The parameters of the model ($\boldsymbol{x}_j$, f_j, a_{ij}) were fitted to maximize the posterior probability of the data:

$$posterior \propto likelihood \cdot prior$$

$$p(model \mid data) \propto p(data \mid model)\, p(model)$$

$$p\left(\left\{\mathbf{x}_j, f_j, a_{ij}\right\} \middle| \left\{n_i(t)\right\}\right) \propto p\left(\left\{n_i(t)\right\} \middle| \left\{\mathbf{x}_j, f_j, a_{ij}\right\}\right) p\left(\left\{\mathbf{x}_j\right\}\right)$$

where $n_i(t)$ is the observed collection of spike times from the i-th RGC.

The likelihood term described how probable the observed spike trains were, given the model. For the computation of likelihood, a linear-nonlinear Poisson model of spike generation was used [6], in which the instantaneous firing rate was given by:

$$\lambda_i(t) = \exp(b_i + \mathbf{k}_i \cdot \mathbf{s}_t)$$

where $\exp(b_i)$ is a baseline spike rate constant fitted separately for each cell, $\boldsymbol{k}_i$ is the spatiotemporal RF, and $\boldsymbol{s}_t$ is the stimulus at time t. For an inhomogeneous Poisson process with rate $\lambda(t)$, the log likelihood of observing the spike train $n(t)$ is [10]:

$$\log p\left(\{n_i(t)\} \middle| \{\mathbf{k}_i\}\right) = \sum_i \sum_t \left(n_i(t) \log \lambda_i(t) - \lambda_i(t)dt\right) + const.$$

Employing the central limit theorem to approximate the distribution of the filtered stimulus values $\boldsymbol{k}_i \cdot \boldsymbol{s}_t$ as Gaussian, it can be shown [11] that the log likelihood depends only on the spike-triggered sum $\mathbf{S}_i$:

$$\log(L) = \log p\left(\{n_i(t)\} \middle| \{\mathbf{k}_i\}\right) \approx$$

$$\sum_i \left[\mathbf{S}_i \cdot \mathbf{k}_i - T \exp\left(b_i + \frac{\sigma^2}{2}\mathbf{k}_i \cdot \mathbf{k}_i\right)\right] + const. \qquad (2)$$

where

$$\mathbf{S}_i = \sum_t n_i(t)\mathbf{s}_t$$

Here T denotes the duration of the experiment, and σ^2 the stimulus variance. Equations (1) and (2) completely specify the likelihood.

The prior probability on cone locations was modeled as a pairwise interaction process [12], reflecting a partial exclusion radius around each cone [13-15]:

$$p\left(\{\mathbf{x}_j\}\right) \propto \prod_{j,j'} h\left(\left\|\mathbf{x}_j - \mathbf{x}_{j'}\right\|\right) \quad (3)$$

where the sigmoid function h sets the expected cone spacing and $\| \boldsymbol{x}_j - \boldsymbol{x}_{j'} \|$ denotes the distance between cones j and j'. To model a typical cone mosaic, h was chosen so that $h(d) = 0$ for $d < d_{min}$, $h(d) = 1$ for $d > d_{max}$, with h rising smoothly between d_{min} and d_{max}. The values of d_{min} and d_{max} were chosen for each retina so that the apparent average inter-cone spacing in the measured RFs matched that of artificial cone maps generated by Gibbs sampling [12] from the prior distribution given in Equation (3). The values were set separately for each cone type; the minimum spacing of S cones was set to be higher than that of L and M cones, reflecting the fact that S cones occur on a sparser lattice [14]. No prior expectations (flat prior) were set for the proportion of cones of different types (f_i) or cone weights (a_i).

For each retina, the model of cones and weights was fitted using a greedy algorithm. At each step the algorithm considered a set of candidate cone locations and cone types, and added the single new cone that would produce the greatest increase in the posterior probability. The set of candidate cones was arranged on a square lattice 3-5 times finer (linear dimensions) than the stimulus pixels. At each location on the lattice there were three candidate cones, one of each type (L, M, and S). For each candidate cone, the change in the posterior associated with adding that cone was computed as follows. First, the weights of the cone in each model RF (a_{ij}) were chosen to maximize the likelihood (i.e., to best match the observed RF). Second, the resulting updated set of model RFs (k_i) was plugged into equation (2) to compute the change in the likelihood, and the chosen location $\boldsymbol{x}_j$ was plugged into equation (3) to compute the change in the prior.

In practice, the first cones to be added were those sampled most strongly by the greatest number of RFs, because those cones yielded the greatest improvement in the match between the model and the data. As the algorithm progressed, it incorporated cones with smaller weights. The procedure was allowed to continue until it appeared that all observed cones had been accounted for, and that additional cones in the model were added at spurious locations, such as regions far from the recording array or in gaps where RGCs were not recorded. The stopping point for the algorithm was set manually for each retina.

Cone classification was verified by checking the sensitivity to the red (R), green (G), and blue (B) display primaries at each cone location (see Fig. 2a-c). In general, each cone contributed to the RF of several RGCs, thus spectral sensitivity estimates were pooled across RGCs. For each RGC that strongly sampled a given cone, the Gaussian profile of the cone was projected onto the red, green and blue display primary contrast values of the STA. This produced a triplet of values summarizing the local spectral sensitivity. These sensitivities were summed across RGCs that strongly sampled the cone by taking the average of the estimated sensitivities, weighted by the SNR of the cell and the weight with which the cone was sampled. Strongly sampled cones were those with a weight that was >3 SD of the distribution of all weights for the given RGC. These triplets were normalized to have a unit length and plotted as points on a sphere (Fig. 2b). Points were colored according to the cone type assigned by the model fit. The centroid of each of the three distinct clusters of points closely matched the expected sensitivities of the L, M and S cones to the three display primaries.

Previous studies have revealed significant variability in the fraction of L, M and S cones across animals and regions of retina [14,16,17]. In the present data, these fractions (for the 7 data sets analyzed in Figure 4k) were: 0.603, 0.326, 0.07; 0.515, 0.411, 0.074; 0.558, 0.399, 0.043; 0.595, 0.375, 0.031; 0.517, 0.46, 0.023; 0.693, 0.284, 0.023; 0.602, 0.351, 0.047. In many data sets S cones were almost certainly under-sampled because incomplete mosaics of SBCs were recorded. The first two preparations listed above had nearly complete SBC mosaics, and in these preparations the cone mosaics contained 7-8% S cones.

Control analysis for cone identification

To control for potential errors in cone identification and classification, an alternate approach was employed and results were compared. The procedure relied on multiple steps to first identify cones and then identify their spectral type, as follows.

For each recorded cell, the frame of the STA with maximum contrast was identified, and this frame was used for further analysis. The first step was to identify pixels that likely represented the input of a cone. From each pixel, the tripet of red, green and blue display primary intensity values was extracted. The similarity of this triplet to the expectation from the spectral sensitivity of each cone type was determined by computing the inner product with the expectation at each pixel. This yielded three images, one for each cone type. Statistically significant pixels were defined as those with intensities that deviated more than 5 SDs from the mean in any of the three images. The noise SD was measured at outlying locations in the display.

Every pixel was then assigned an intensity equal to the sum of the absolute values of its inner products with the expectations from each cone type. Among the significant pixels, local maxima were identified as pixels with higher intensity than all 8 neighboring pixels. For each local maximum, a preliminary estimate of cone location was taken as the center of mass of a region including the immediately adjacent pixels. These estimates were pooled across all STAs. Because each cone was sampled by multiple cells, each cone location had multiple location estimates. Estimates of the same cone were identified by spatial clustering of their locations. Two estimates were put in the same cluster if they were closer than 1.2 pixels. In rare cases (< 2%), a single cluster seemed to contain estimates of two distinct cones. Any cluster with two estimates at least 1.6 pixels apart were split into two sub-clusters; this operation was applied iteratively for the resulting sub-clusters. After defining and splitting clusters, estimates in each cluster were averaged to produce a single estimate for the location of each cone.

This initial estimate was used in a multi-parameter fit that yielded the final estimate of the cone location and type. The STAs of the cells which had been identified as sampling the cone were used to fit a 2-dimensional Gaussian function with width (SD) of 0.75 pixels. The location of the Gaussian, as well as sensitivity to each display primary, were allowed to vary, yielding the final location and spectral parameters for the cone. Cones were labeled as L, M, or S by classifying their sensitivities to the display primaries in a three dimensional space (e.g. Fig. 2b) using k-means clustering.

The results of the alternate procedure were then compared to the results of the standard procedure. Fig. 5 shows an overlay of the cone mosaics found with the two procedures; mismatching cone types are represented by dots with two colors. A small number of identified cones differed in the two procedures. Fig. 7b shows the purity analysis performed with cones identified using the alternate procedure, using all the same data sets and identical analysis as Fig. 4k. The alternate procedure had no significant effect on the finding of non-random purity in midget cells.

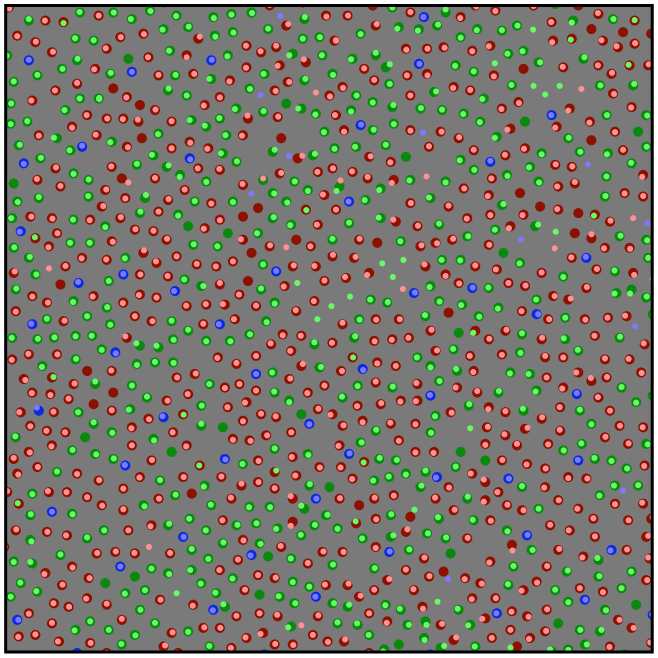

Figure 5. Comparison of standard and alternate cone identification procedures. The image shows a subset of a cone mosaic identified with the standard and alternate procedures (see Supplementary Methods). Each cone identified with the new (old) procedure is represented by a large (small) disk, the color of which represent the cone type classification. A total of 1,882 cones were identified in common between the two procedures. Of these, 65 cones were identified as having different spectral types in the two procedures. The standard procedure identified 160 cones not found in the alternate procedure, and the alternate procedure identified 199 cones not found in the standard procedure.

Cones providing input to receptive field center and surround

To analyze cone sampling by the RF center and surround, cones were identified as contributing primarily to the center or surround, respectively. This definition was operational: the mechanisms producing the RF center and surround are in fact largely overlapping (see [18]), therefore, many cones (particularly cones in the middle of the RF) must in fact contribute to both center and surround. Cones were identified as contributing primarily to center and surround based on their spatial location and the net sign of their contribution to light response, as follows. Cones in the RF center were defined as those with a weight greater than or equal to 10% of the weight of cone with the largest weight (which is by definition in the center), with the same sign, and within 3 median cone spacings from another center cone. Surround cones were defined as those cones with a light response polarity opposite to the center, weights >0.5% that of the peak cone but of opposite sign, and within 8 SDs of a circular Gaussian fit to the RF center.

As a control, an alternate definition of surround cones was also tested. In this definition all cones within 8 SDs of the RF center that were not identified as center cones were considered surround cones. Using this alternate definition yielded results very similar to Fig. 4l (not shown).

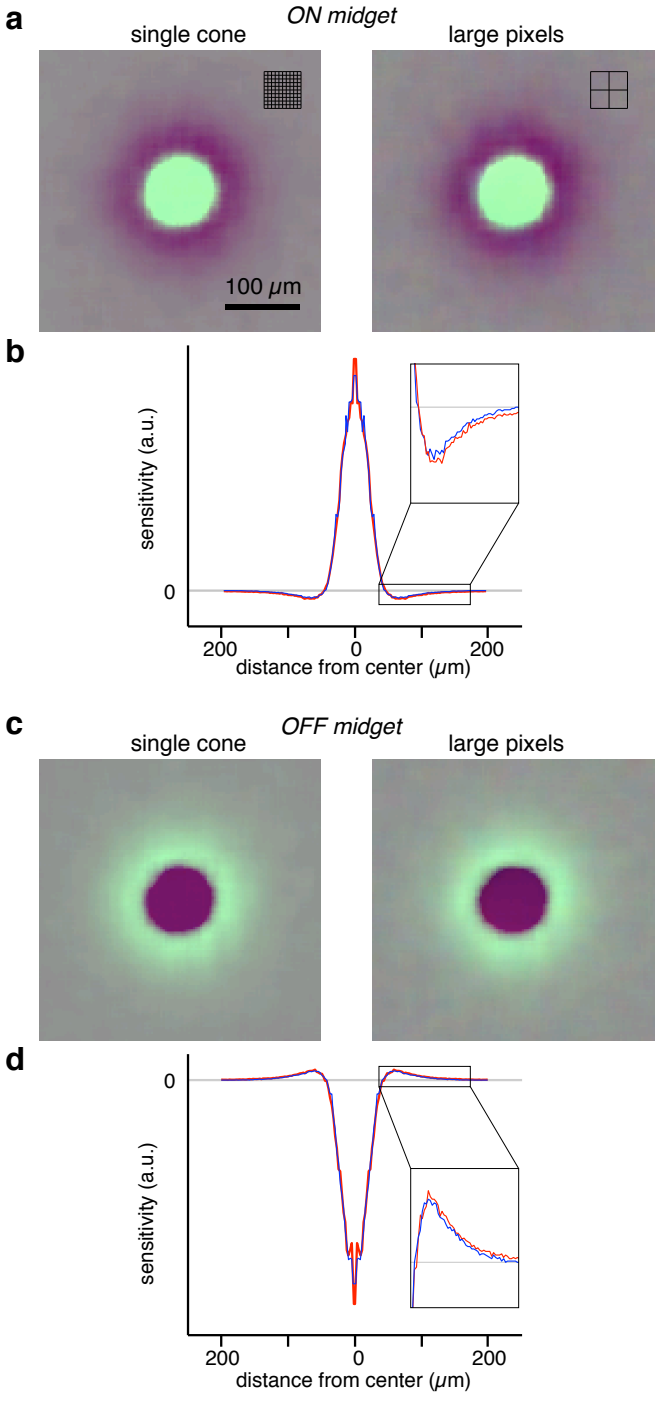

Figure 6. Comparison of RF structure estimated using single cone and conventional measurements. For ON and OFF midget cells in a single retina, RF measurements were performed using small and large pixels. From the small pixel data, cones were identified and their spatial locations and profiles measured and the weights of their inputs estimated (see Supplementary Methods). From the large pixel data, the raw values of the STA at each pixel location were used for RF estimates. In both cases, RFs of all cells of a type were re-centered and averaged to produce a standard RF for each cell type. (a) Average RF for ON midget cells. Insets show pixel sizes. Contrast in the images is saturated in the center of the RF in order to emphasize the spatial structure of the surround. (b) Average RF profile for ON midget cells; inset shows an expanded representation of the surround. (c,d) Similar to (a) and (b), but for OFF midget cells.

Weights on cones in the RF surround were weaker than those in the center, as expected. To verify that the estimates of the RF center and surround cone weights were not biased, RFs of ON and OFF midget cells obtained with identified cones and with standard coarse pixellated measurement (e.g. [2]) were compared (Fig. 6). The RFs obtained using the two approaches were nearly identical, consistent with the idea that fine-grained mapping combined with cone identification and weight estimation yielded unbiased estimates of the RF.

S cone input to midget and parasol cells

The frequency with which S cones were strongly sampled by ON and OFF parasol and midget cells was estimated as follows. First, S cones were identified using the STAs of small bistratified cells. For parasol and midget cells, S cones which fell within the 1 SD contour of a circular Gaussian fit to the RF were examined. This area was chosen to highlight the region of the RF with the most reliable estimates of S cone input. If the weight on an S cone exceeded 15% of the weight of the strongest cone input to the RGC, that S cone was considered to be strongly sampled. The frequency of S cone sampling was defined as the ratio of the number of strongly sampled S cones to the total number of S cones, within the 1 SD contour. Results were pooled across all cells in the 4 preparations in which many small bistratified cells were recorded; 3 data sets with less reliable information about S cones were excluded from analysis.

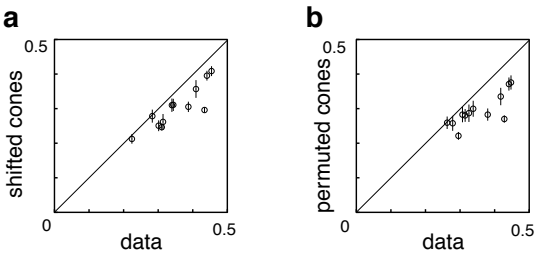

Figure 7. Controls for purity analysis. Each panel shows an alternative analysis of cone type purity in midget cell RFs. Purity values computed with and without manipulation of the underlying cone mosaic are represented, in the same format as Figure 4k. (a) Analysis of cone type purity performed with shifted cone mosaics rather than artificially clumped cone mosaics (see Methods). (b) Analysis of cone type purity performed with cones identified and classified using the alternative procedure (see Supplementary Methods).

The results of the analysis were mostly, but not entirely, independent of the threshold used for S cone sampling. As expected, the apparent sampling frequency of S cones increased as the threshold was varied from 100% to 0.1% of the weight of the strongest cone input. At the threshold value of 15% used in the main analysis (Fig 4d), OFF midget cells frequently sampled S cones but the other cell types did not, leading to the conclusion that only this cell type received frequent, substantial inputs from S cones. However, for threshold values below 5% there was an indication of S cone input to ON midget cells that, while less frequent than the input to OFF midget cells, was more frequent than the apparent sampling by parasol cells. This finding was consistent with a separate analysis in which the summed input of S cones was computed for cells of all four types with RFs that encompassed at least one known S cone. In this analysis, parasol cells exhibited little or no summed S cone input, ON midget cells exhibited weak summed input (~1%), and OFF midget cells exhibited significantly stronger summed input (~3-5%). At the threshold values below 1%, many spurious S cone inputs were identified by the sampling analysis, but there was a suggestion of very weak S cone inputs to parasol cells.

The weights of S cones tended to be 10-50% of the weights of L or M cones at similar radial distances in the RF. These diminished weights may reflect diminished function of S cones relative to L and M cones in the in vitro preparation. Alternatively, they may reflect weaker sampling of the S cones than of the L or M cones by the bipolar cells which carry S cone signals to the OFF midget cells, a phenomenon observed in ground squirrel retina [19]. Finally, the smaller S cone input could result from the lower mean photon absorption rates in S cones compared to L and M cones in the present conditions (see above). In the data analyzed, S cone input to midget cells was stable for at least several hours, and sensitivity of small bistratified cells to modulation of S cones was stable for 6-10 hours.

Supplementary Discussion

Preceding findings on S cone input to midget and parasol cells

The possibility of S cone input to parasol cells and their associated presynaptic circuitry has received considerable attention. One early study of magnocellular neurons in the LGN (the post-synaptic targets of parasol cells) suggested they may receive S cone input (see [8], Fig. 6). However, it is possible that some of the neurons in this data set were koniocellular cells, which are now appreciated as a separate pathway for S cone signals in the brain. Also, early work that associated parasol cell physiology with the psychophysically defined photopic luminosity function indicated that S cone input was avoided by parasol cells [20-22]. A more recent study indicated that the fractional input to magnocelular neurons in LGN provided by S cones was similar to the fraction of S cones in the retina [23], suggesting that parasol cells sample from all three cone types indiscriminately. Subsequent physiological investigations did not reveal significant S cone input to parasol cells, suggesting that the previous result reflected errors in generating cone isolating stimuli [24,25]. Finally, a recent anatomical study indicated that S cones provide input to the diffuse bipolar cells that connect to parasol cells, although it may be weaker than the input of L/M cones [26].

The possibility of S cone input to midget cells, and to their parvocellular target neurons in the LGN, has also been debated. Early investigations of color opponent neurons in the LGN did not distinguish between parvocellular and koniocellular units [8,27]. A

specialized blue-yellow opponent RGC type and an associated geniculate pathway was not appreciated until much later [28,29]. Several recent studies have not revealed S cone input to the RF center of midget cells or parvocellular neurons [24,25,30,31]. However, anatomical evidence indicates that OFF midget bipolar cells form synapses with S cones in the primate retina [32].

Preceding findings on the purity of L/M cone input to midget cells

Preceding studies have suggested a number of possibilties regarding the nature of L and M cone inputs to midget cells, in both the RF center and surround. Early work highlighted the color opponent properties of (probable) midget cells [27,33-35] and revealed a wide range of color tuning in parvocellular neurons in the LGN [8]. These findings set the stage for a vigorous investigation of the circuitry of color vision in the retina, exploiting anatomical approaches and cone isolating stimuli to selectively activate different cone types in physiological experiments (see [34,36-40]).

Near the fovea, the anatomical observation that an individual midget RGC receives primary excitatory input from a single bipolar cell which is in turn connected to a single cone [41] revealed that cone type purity can emerge in the RF center without any specific connectivity. However, other studies suggested that midget cells that receive input from several cones may also exhibit some degree of purity. One study showed that midget cells received either a small number, or instead a large number, of midget bipolar cell contacts, distributed in a bimodal fashion across cells, suggestive of a structural distinction between the inputs of bipolar cells receiving L vs. M cone input [42]. This hypothesis has never been tested physiologically, and subsequent work in marmosets did not reveal any structural specificity [43]. It was also observed that midget RGC dendritic arbors exhibit striking clustering and asymmetry, possibly consistent with specific sampling of inputs from one cone type or another in the cone mosaic; quantitative analysis supported this possibility [44]. However, this interpretation is complicated by the fact that similar clustering is observed in midget cells of dichromatic primates that have only S cones and one long/medium wavelength sensitive cone type [45], and is not observed in trichromatic marmosets [46]. The findings supporting cone type purity in the RF center appear to be at odds with recordings from midget, parasol and horizontal cells made at same retinal location, which were consistent with random sampling [17].

Cone type purity of the RF surround has also been debated. Modeling work suggested that random sampling in the RF surround was sufficient to explain the color-opponent properties of LGN neurons [47]. However, evidence for cone type purity in the RF surround was suggested in early work with cone isolating stimuli [48], a finding that was partly supported in follow-up work but with some limitations in spatial resolution [30]. More recent work in the mid-peripheral retina broadly supported this view [49], suggesting that the surround may be biased in favor of inputs from cones of the type that is not dominant in the RF center. The suggestion of cone type purity in the surround is surprising in light of the putative role of horizontal cells in forming the surround: anatomical evidence indicates that in primates neither of the two types of horizontal cells (H1 and H2) exhibit any selectivity for L vs. M cones [50].

Motivation for new methods

Two technical considerations in previous work suggest that a new approach may be useful in determining the L/M cone input specificity in midget cells.

First, the main tool for identifying the inputs from different cone types to a given RGC has been modulation of the spectral content of the stimulus in a manner intended to isolate the contributions of a single cone type (L, M, or S) [7]. Although theoretically elegant, this technique is sensitive to small errors in spectral calibration, non-uniformities or non-linearity in stimulus displays, optical elements between the stimulus and the photoreceptors including macular pigment and cornea, and small uncertainties in the measured spectral absorption of the cones. These uncertainties are amplified by the substantial overlap in the L and M cone spectral absorption curves, so that errors that are small on a wavelength basis can translate into large errors in cone isolation. Typically, for a stimulus that is intended to isolate either the L or M cones while not stimulating the other type, the true magnitude of excitation of the selected cone type relative to the cone type to be silenced is probably on the order of 5:1, in the best cases 10:1 [1] (G.D. Field & E.J. Chichilnisky, unpublished observations). Therefore, spectral methods for cone isolation may not be reliable. Furthermore, even in the idealized case, purely spectral methods isolate a type of cone but not an individual cone, and therefore do not reveal the spatial pattern of cone inputs.

Second, tests of random connectivity between RGCs and L/M cones are subject to a major consideration that is rarely treated because the underlying data are inaccessible: the possibility of clumping or other non-random structure in the cone mosaic. For example, if L or M cones tend to aggregate with cones of the same type in the cone mosaic, then truly random sampling of the collection of cones in the vicinity of a given RGC would be expected to produce a non-random degree of cone type purity in the RF center. If the surround is also random, but much larger and therefore reflecting a roughly even mix of L/M cone input, then an unusual degree of color opponency between center and surround would be expected. For these reasons, any test of whether L/M cones are sampled randomly by midget cells requires knowledge of the structure of the underlying cone mosaic.

The methods presented here bypass these technical issues. Spectral isolation is not necessary: the cones are separated by their spatial locations, and at one location there is only one cone (Fig. 1b). Therefore the only potential error is mis-classifying a particular cone; the error rate for this is low (Fig. 2b,c). Measurement of the underlying cone mosaic (Fig. 2e), and of the effective connections of RGCs to each cone (Fig. 2h), permit a clearly defined statistical test of non-random connectivity, because the predictions of random connectivity are easily and robustly simulated while keeping other factors constant by permuting L and M cone labels (Fig. 4k,l). The purity of center and surround in the RF are investigated separately, using the same logic (Fig. 4k,l). The effects of clumping in the mosaic are also easily incorporated in the analysis, because random relabeling of L and M cones can be done in a manner that simulates the degree of clumping in the real cone mosaic (Fig. 4m). Finally, because cones are identified individually and the strengths of their inputs are known, further tests can be used to determine the role of specific sampling vs. specific weighting of inputs (Fig. 4n,o).

References

1. Chichilnisky, E. J. & Baylor, D. A. Receptive-field microstructure of blue-yellow ganglion cells in primate retina. *Nat Neurosci* **2**, 889-893 (1999).
2. Field, G. D. et al. Spatial properties and functional organization of small bistratified ganglion cells in primate retina. *J Neurosci* **27**, 13261-13272 (2007).
3. Litke, A. M. et al. What does the eye tell the brain? Development of a system for the large scale recording of retinal output activity. *IEEE Trans Nucl Sci* **51**, 1434-1440 (2004).
4. Field, G. D. et al. High-sensitivity rod photoreceptor input to the blue-yellow color opponent pathway in macaque retina. *Nat Neurosci* **12**, 1159-1164 (2009).
5. Baylor, D. A., Nunn, B. J. & Schnapf, J. L. Spectral sensitivity of cones of the monkey Macaca fascicularis. *J Physiol* **390**, 145-160 (1987).
6. Chichilnisky, E. J. A simple white noise analysis of neuronal light responses. *Network* **12**, 199-213 (2001).
7. Estevez, O. & Spekreijse, H. The "silent substitution" method in visual research. *Vision Res* **22**, 681-691 (1982).
8. Derrington, A. M., Krauskopf, J. & Lennie, P. Chromatic mechanisms in lateral geniculate nucleus of macaque. *J Physiol* **357**, 241-265 (1984).
9. Chichilnisky, E. J. & Kalmar, R. S. Functional asymmetries in ON and OFF ganglion cells of primate retina. *J Neurosci* **22**, 2737-2747 (2002).
10. Snyder, D. & Miller, M. *Random Point Processes in Time and Space* (Springer-Verlag, 1991).
11. Paninski, L. Maximum likelihood estimation of cascade point-process neural encoding models. *Network* **15**, 243-262 (2004).
12. Moeller, J. & Waagepetersen, R. *Statistical inference and simulation for spatial point processes.* (Chapman Hall, 2004).
13. Wassle, H. & Riemann, H. J. The mosaic of nerve cells in the mammalian retina. *Proc R Soc Lond B Biol Sci* **200**, 441-461 (1978).
14. de Monasterio, F. M., Schein, S. J. & McCrane, E. P. Staining of blue-sensitive cones of the macaque retina by a fluorescent dye. *Science* **213**, 1278-1281 (1981).
15. Curcio, C. A., Sloan, K. R., Kalina, R. E. & Hendrickson, A. E. Human photoreceptor topography. *J Comp Neurol* **292**, 497-523 (1990).
16. Roorda, A. & Williams, D. R. The arrangement of the three cone classes in the living human eye. *Nature* **397**, 520-522 (1999).
17. Diller, L. et al. L and M cone contributions to the midget and parasol ganglion cell receptive fields of macaque monkey retina. *J Neurosci* **24**, 1079-1088 (2004).
18. Rodieck, R. W. *The first steps in seeing* (Sinauer, Sunderland, MA, 1998).
19. Li, W. & DeVries, S. H. Bipolar cell pathways for color and luminance vision in a dichromatic mammalian retina. *Nat Neurosci* **9**, 669-675 (2006).
20. Lee, B. B., Martin, P. R. & Valberg, A. The physiological basis of heterochromatic flicker photometry demonstrated in the ganglion cells of the macaque retina. *J Physiol* **404**, 323-347 (1988).
21. Kaiser, P. K., Lee, B. B., Martin, P. R. & Valberg, A. The physiological basis of the minimally distinct border demonstrated in the ganglion cells of the macaque retina. *J Physiol* **422**, 153-183 (1990).
22. Lee, B. B., Pokorny, J., Smith, V. C. & Kremers, J. Responses to pulses and sinusoids in macaque ganglion cells. *Vision Res* **34**, 3081-3096 (1994).
23. Chatterjee, S. & Callaway, E. M. S cone contributions to the magnocellular visual pathway in macaque monkey. *Neuron* **35**, 1135-1146 (2002).
24. Sun, H., Smithson, H. E., Zaidi, Q. & Lee, B. B. Specificity of cone inputs to macaque retinal ganglion cells. *J Neurophysiol* **95**, 837-849 (2006).
25. Tailby, C., Szmajda, B. A., Buzas, P., Lee, B. B. & Martin, P. R. Transmission of blue (S) cone signals through the primate lateral geniculate nucleus. *J Physiol* **586**, 5947-5967 (2008).
26. Lee, S. C. & Grunert, U. Connections of diffuse bipolar cells in primate retina are biased against S-cones. *J Comp Neurol* **502**, 126-140 (2007).
27. Wiesel, T. N. & Hubel, D. H. Spatial and chromatic interactions in the lateral geniculate body of the rhesus monkey. *J Neurophysiol* **29**, 1115-1156 (1966).
28. Dacey, D. M. & Lee, B. B. The 'blue-on' opponent pathway in primate retina originates from a distinct bistratified ganglion cell type. *Nature* **367**, 731-735 (1994).
29. Martin, P. R., White, A. J., Goodchild, A. K., Wilder, H. D. & Sefton, A. E. Evidence that blue-on cells are part of the third geniculocortical pathway in primates. *Eur J Neurosci* **9**, 1536-1541 (1997).
30. Reid, R. C. & Shapley, R. M. Space and time maps of cone photoreceptor signals in macaque lateral geniculate nucleus. *J Neurosci* **22**, 6158-6175 (2002).
31. Solomon, S. G., Lee, B. B., White, A. J., Ruttiger, L. & Martin, P. R. Chromatic organization of ganglion cell receptive fields in the peripheral retina. *J Neurosci* **25**, 4527-4539 (2005).
32. Klug, K., Herr, S., Ngo, I. T., Sterling, P. & Schein, S. Macaque retina contains an S-cone OFF midget pathway. *J Neurosci* **23**, 9881-9887 (2003).
33. Jacobs, G. H. & De Valois, R. L. Chromatic opponent cells in squirrel monkey lateral geniculate nucleus. *Nature* **206**, 487-489 (1965).
34. De Valois, R. L., Abramov, I. & Jacobs, G. H. Analysis of response patterns of LGN cells. *J Opt Soc Am* **56**, 966-977 (1966).
35. de Monasterio, F. M., Gouras, P. & Tolhurst, D. J. Trichromatic colour opponency in ganglion cells of the rhesus monkey retina. *J Physiol* **251**, 197-216 (1975).
36. Lee, B. B. Receptive field structure in the primate retina. *Vision Res* **36**, 631-644 (1996).
37. Dacey, D. M. Parallel pathways for spectral coding in primate retina. *Annu Rev Neurosci* **23**, 743-775 (2000).
38. Gegenfurtner, K. R. Cortical mechanisms of colour vision. *Nat Rev Neurosci* **4**, 563-572 (2003).
39. Solomon, S. G. & Lennie, P. The machinery of colour vision. *Nat Rev Neurosci* **8**, 276-286 (2007).
40. Lee, B. B. Neural models and physiological reality. *Vis Neurosci* **25**, 231-241 (2008).
41. Kolb, H. & Dekorver, L. Midget ganglion cells of the parafovea of the human retina: a study by electron microscopy and serial section reconstructions. *J Comp Neurol* **303**, 617-636 (1991).
42. Calkins, D. J., Schein, S. J., Tsukamoto, Y. & Sterling, P. M and L cones in macaque fovea connect to midget ganglion

cells by different numbers of excitatory synapses. *Nature* **371**, 70-72 (1994).
43. Jusuf, P. R., Martin, P. R. & Grunert, U. Random wiring in the midget pathway of primate retina. *J Neurosci* **26**, 3908-3917 (2006).
44. Martin, P. R., Lee, B. B., White, A. J., Solomon, S. G. & Ruttiger, L. Chromatic sensitivity of ganglion cells in the peripheral primate retina. *Nature* **410**, 933-936 (2001).
45. Yamada, E. S., Silveira, L. C. & Perry, V. H. Morphology, dendritic field size, somal size, density, and coverage of M and P retinal ganglion cells of dichromatic Cebus monkeys. *Vis Neurosci* **13**, 1011-1029 (1996).
46. Ghosh, K. K., Goodchild, A. K., Sefton, A. E. & Martin, P. R. Morphology of retinal ganglion cells in a new world monkey, the marmoset Callithrix jacchus. *J Comp Neurol* **366**, 76-92 (1996).
47. Lennie, P., Haake, W. & Williams, D. R. in *Computational models of visual processing* (eds Landy, M. & Movshon, J. A.) 71-82 (MIT Press, 1991).
48. Reid, R. C. & Shapley, R. M. Spatial structure of cone inputs to receptive fields in primate lateral geniculate nucleus. *Nature* **356**, 716-718 (1992).
49. Buzas, P., Blessing, E. M., Szmajda, B. A. & Martin, P. R. Specificity of M and L cone inputs to receptive fields in the parvocellular pathway: random wiring with functional bias. *J Neurosci* **26**, 11148-11161 (2006).
50. Dacey, D. M., Lee, B. B., Stafford, D. K., Pokorny, J. & Smith, V. C. Horizontal cells of the primate retina: cone specificity without spectral opponency. *Science* **271**, 656-659 (1996).